7. Other Phenomena

7.1. Sea Ice

Sea ice around Japan is observed mainly in the Sea of Okhotsk and the Strait of Tartary. Its reflectance is similar to that of clouds, appearing in visible imagery as shades of grey – specifically light grey in the northern Sea of Okhotsk due to lower reflection relating to the area's high latitude and small solar elevation angles. As a result, sea ice areas may be mistaken for low clouds, but can easily be discriminated in animations due to its slower movement.

Figure 7-1-1 shows B03 visible image of sea ice east of Sakhalin Oblast and to the northeast of Hokkaido. This is easier to discriminate than in B13 infrared image from the same period (Fig. 7-1-2) due to lower temperature differences from the surrounding sea surface.
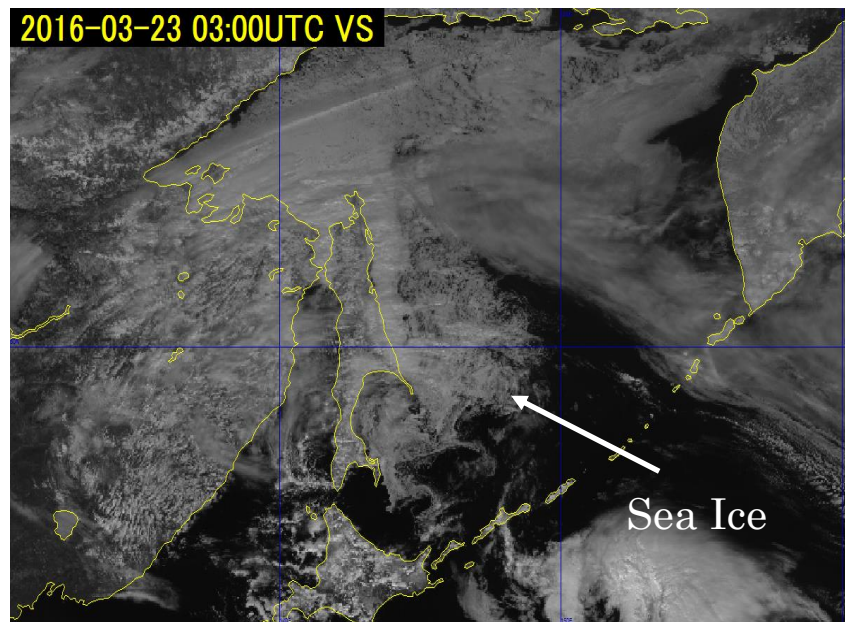

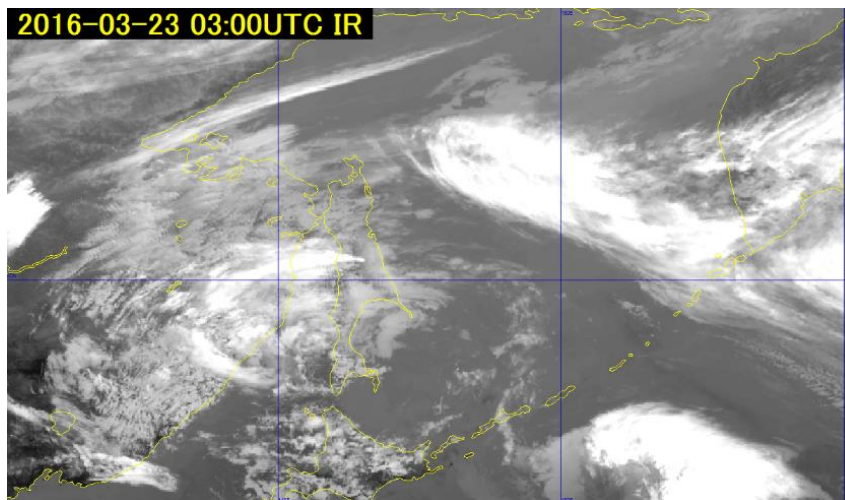Fig. 7-1-1. B03 visible image for 03:00 UTC on 23 March 2016

Fig. 7-1-2. B13 infrared image for 03:00 UTC on 23 March 2016

The Himawari-8 satellite Natural Color RGB composite image in Figure 7-1-3 for 05:00 UTC on 23 March 2016 shows a swirl of sea ice roughly 15 km in diameter north of the Shiretoko Peninsula, with display in cyan for easy discrimination from clouds. The vortex pattern observed is attributed to currents or wind. The swirl as a whole is too large to see from the sea or land surface, but is clear in aviation or satellite observation. Sea ice condition charts based on such imagery are issued for safety in maritime operations.
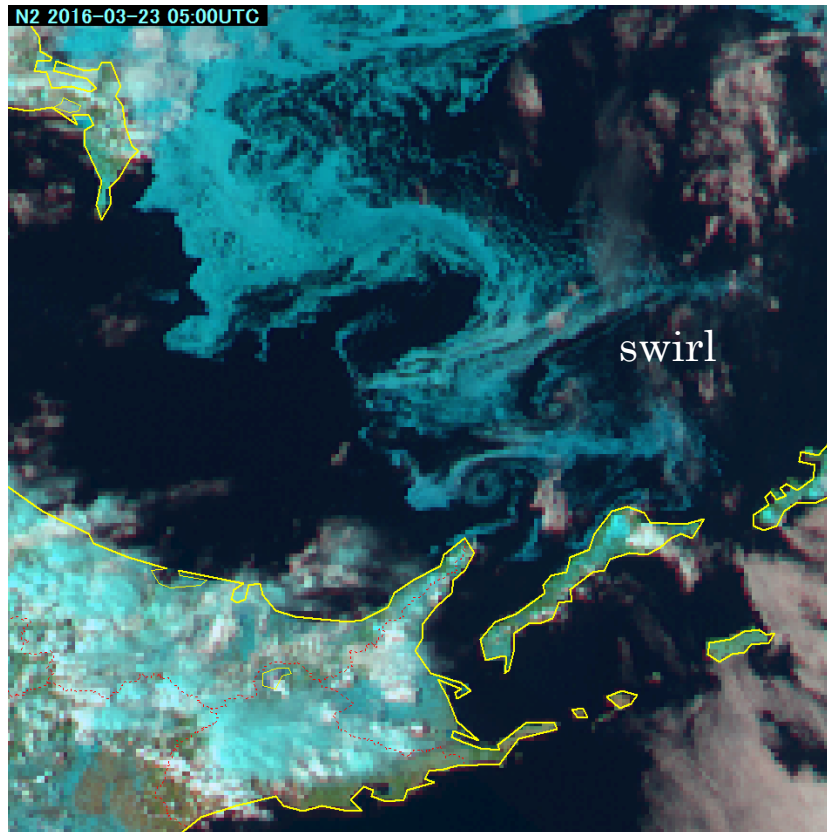

Fig. 7-1-3. Day Natural Color RGB composite image for 05:00 UTC on 23 March 2016

7.2. Snow

Snow-covered areas are displayed as white in B03 visible imagery due to high sunlight reflectance. Although identification of such areas can be challenging due to minimal temperature differences from surrounding areas, their relatively constant appearance over periods of a few days in visible imagery allows discrimination from clouds and snowfall.

Figure 7-2-1 shows B03 visible image for 19 January 2016, with mostly clear skies in the Kanto district revealing snow in white across Tokyo, Saitama, Gunma and Tochigi. Snow and clouds both appear in white, making discrimination in still imagery difficult. Discrimination is also problematic due to minimal temperature differences in the infrared imagery of Figure 7-2-2 for the same period.
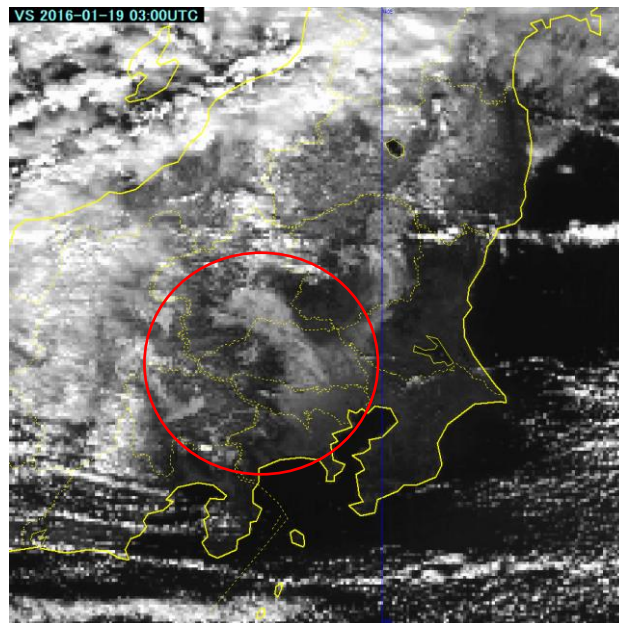
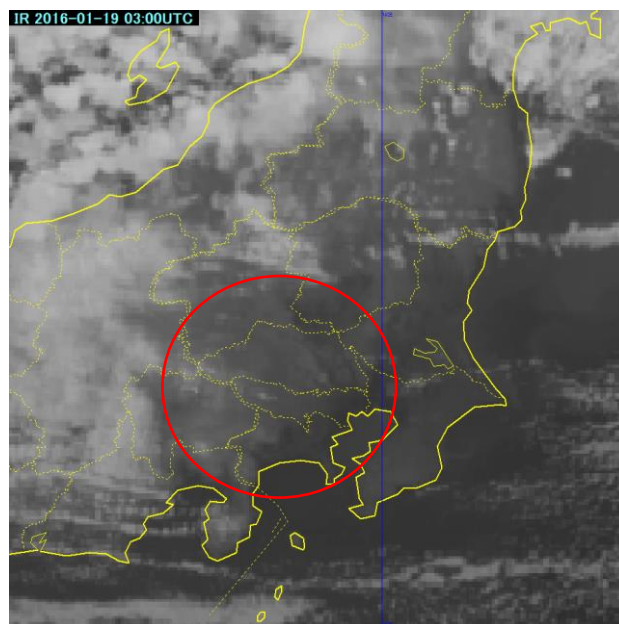Fig. 7-2-1. Visible image for 03:00 UTC on 19 January 2016

Fig. 7-2-2. Infrared image for 03:00 UTC on 19 January 2016

Figure 7-2-3 shows a Natural Color RGB composite of near-infrared and visible imagery for the same period. In the near-infrared band of B05 with an observation wavelength of 1.6 μm, the lower sunlight reflectance of ice allows discrimination from water. In Natural Color RGB composite imagery, ice crystals in upper clouds, snow areas and sea ice are all shown in cyan, enabling identification of snow areas.

Vegetation is shown in green, land surfaces in brown, and cloud/fog water particles in white.
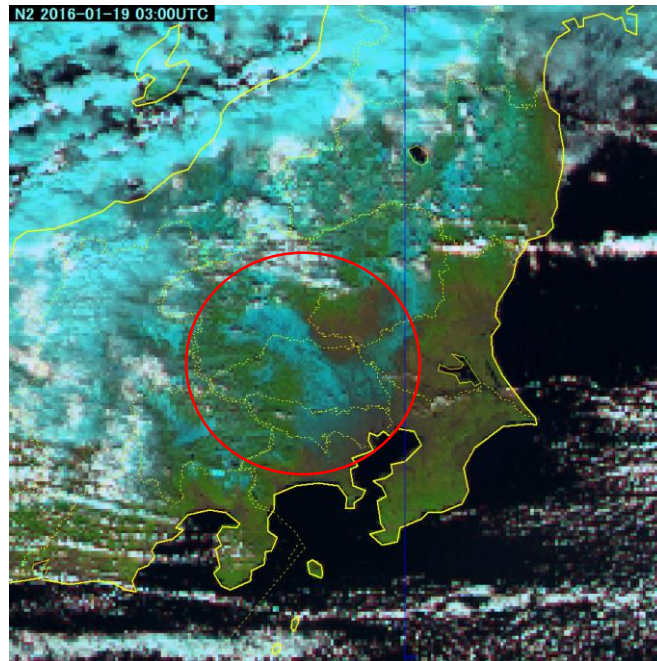

Fig. 7-2-3. Natural Color RGB composite image for 03:00 UTC on 19 January 2016

7.3. Aeolian Dust

Figures 7-3-1 – 7-3-4 show Himawari-8 image of Aeolian dust (a.k.a. yellow dust/Kosa, which is conveyed along atmospheric currents from the Gobi Desert and the Taklamakan Desert in China) whipped up by strong cyclone-related winds around the Gobi Desert for 09:30 UTC on 9 June 2015. Figure 7-3-1 is B03 visible image showing dust spiraling up in grey, whereas True Color Reproduction RGB and Natural Color RGB composite imagery shows the dust in brown (Figs. 7-3-2 and 7-3-3, respectively). Dust RGB composite imagery specifically designed for Aeolian dust monitoring shows the phenomenon in magenta, highlighting dispersive wind-related flows.
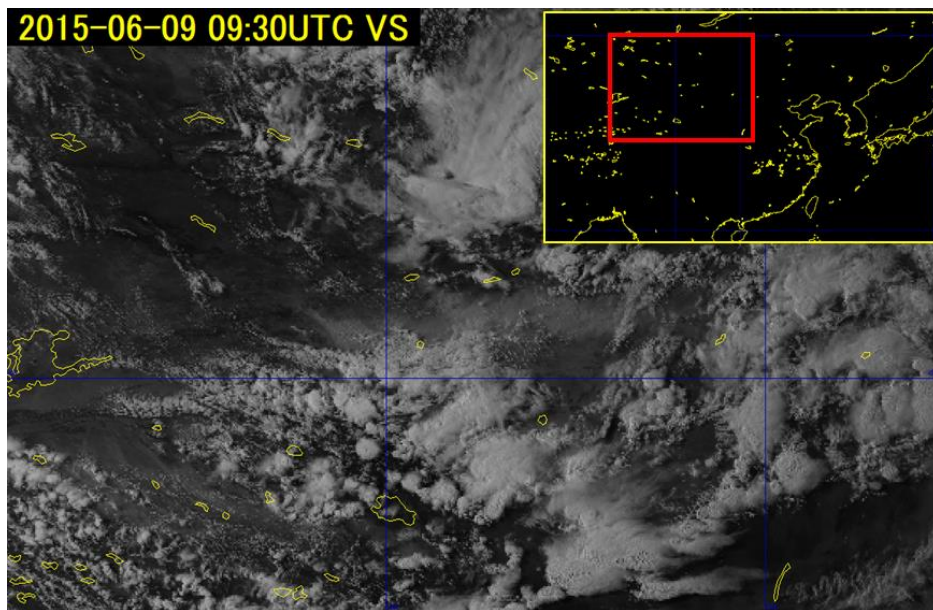

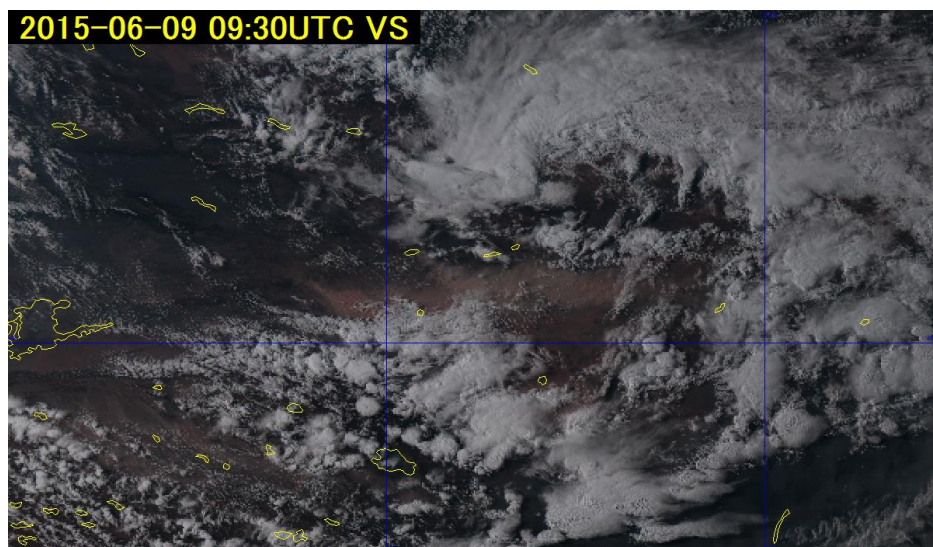Fig. 7-3-1. B03 visible image for 09:30 UTC on 9 June 2015

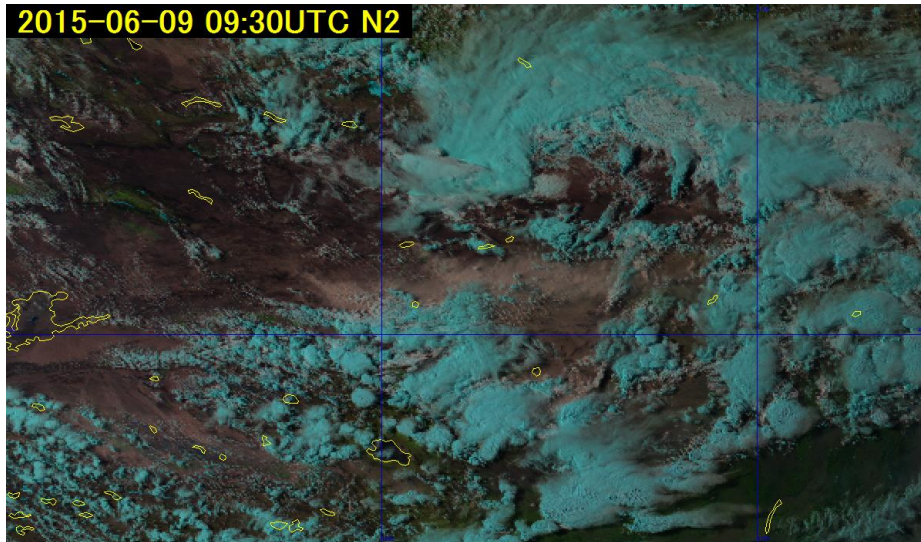Fig. 7-3-2. True Color Reproduction RGB composite image for 09:30 UTC on 9 June 2015

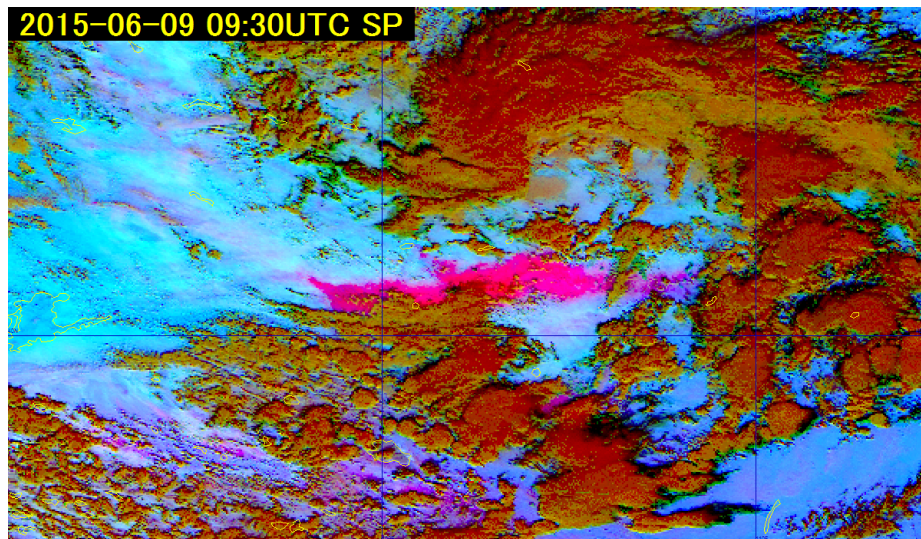Fig. 7-3-3. Natural Color RGB composite image for 09:30 UTC on 9 June 2015

Fig. 7-3-4. Dust RGB composite image for 09:30 UTC on 9 June 2015

Figure 7-3-5 shows B03 visible image, Fig. 7-3-6 shows True Color RGB composite image, Figure 7-3-7 shows Natural Color RGB composite image, and Figure 7-3-8 shows Dust RGB composite image of Aeolian dust reaching the area around Japan for 03:00 UTC on 7 March 2016. The latter shows the dust particularly clearly in magenta.
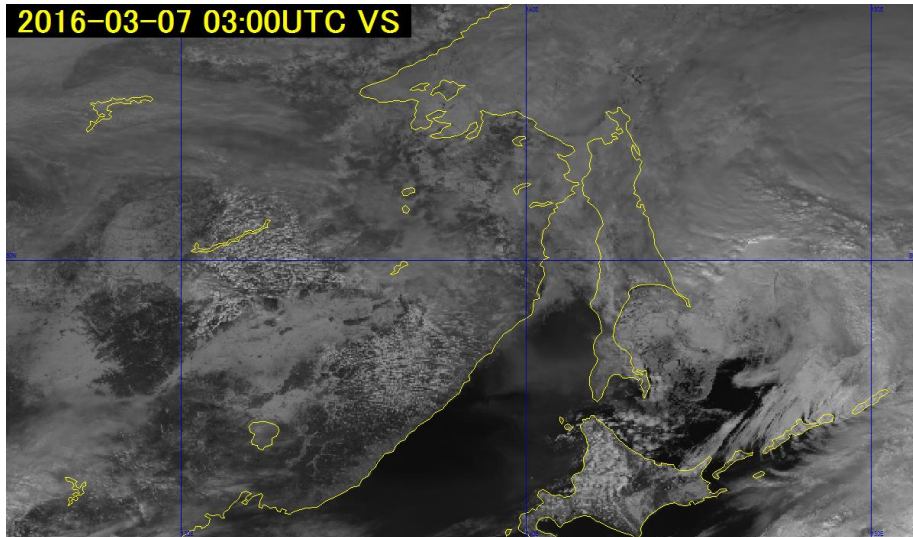
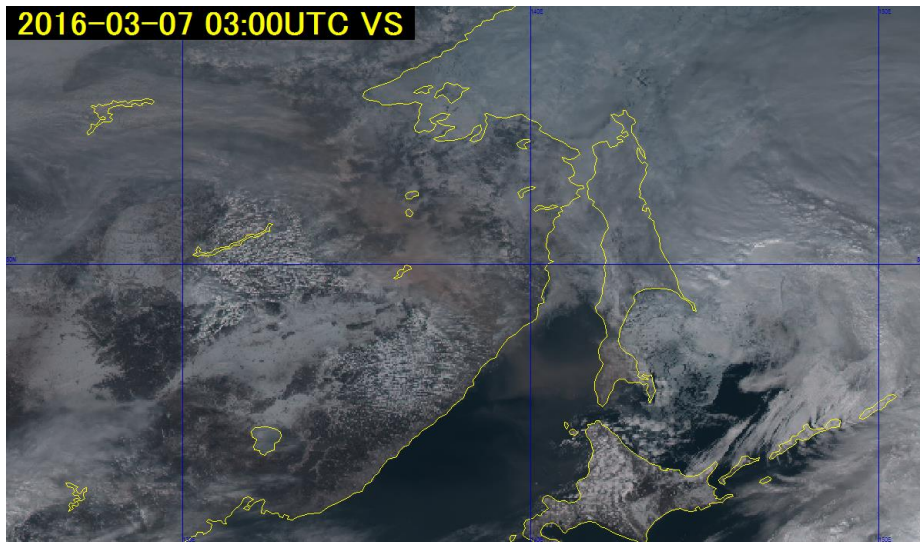Fig. 7-3-5. B03 visible image for 03:00 UTC on 7 March 2016

Fig. 7-3-6. True Color Reproduction RGB composite image for 03:00 UTC on 7 March 2016
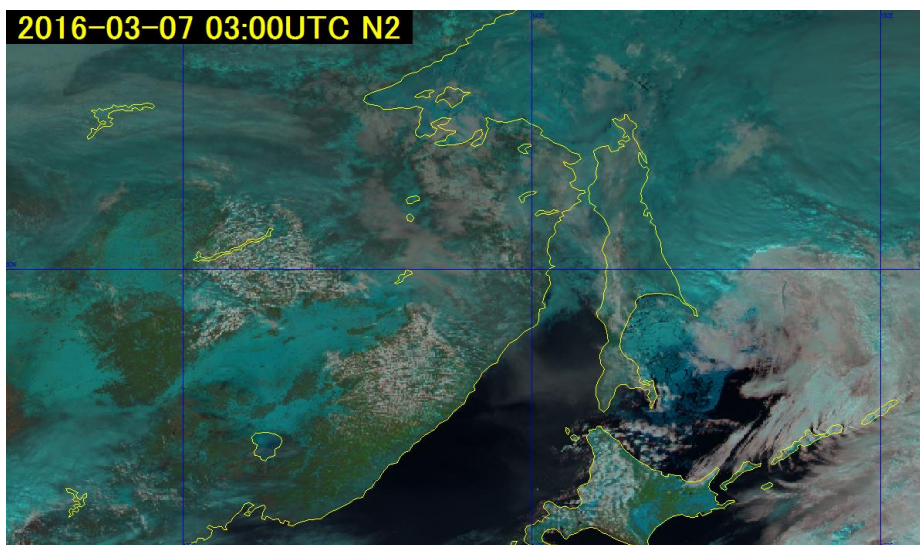

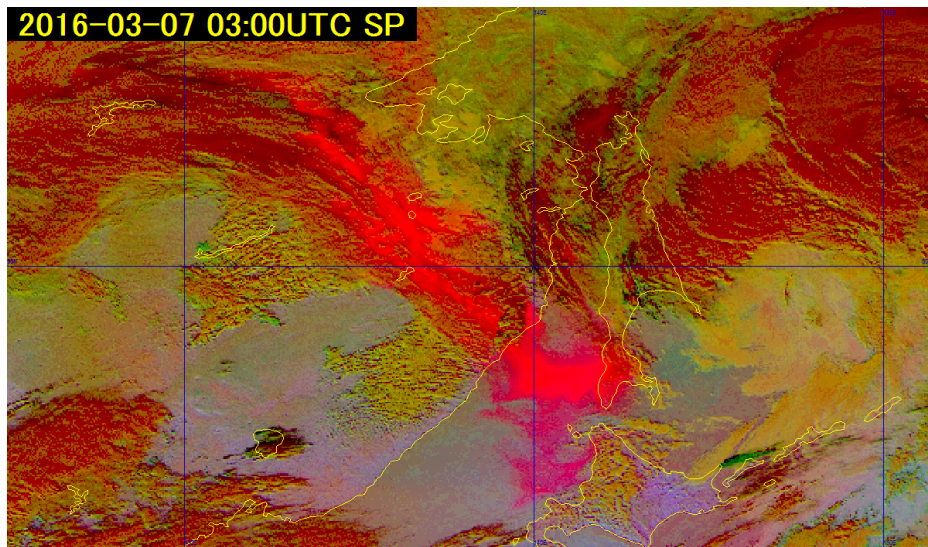Fig. 7-3-7. Natural Color RGB composite image for 03:00 UTC on 7 March 2016

Fig. 7-3-8. Dust RGB composite image for 03:00 UTC on 7 March 2016

7.4.Volcanic Eruptions

Volcanic eruptions produce wind-dispersed plumes of potentially toxic ash and gas that can also adversely affect aviation safety, giving rise to a need for related prediction. In this context, data from several Himawari-8 satellite observation bands are analyzed to clarify volcanic ash and gas movement. Figure 7-4-1 shows True Color Reproduction image for a volcanic eruption on Kuchinoerabu Island at 02:10 UTC on 29 May 2015. While volcanic plumes are difficult to distinguish from surrounding clouds in monotone visible imagery, a visible imagery combination shows brownish plume content spreading westward and east-southeastward of the island.
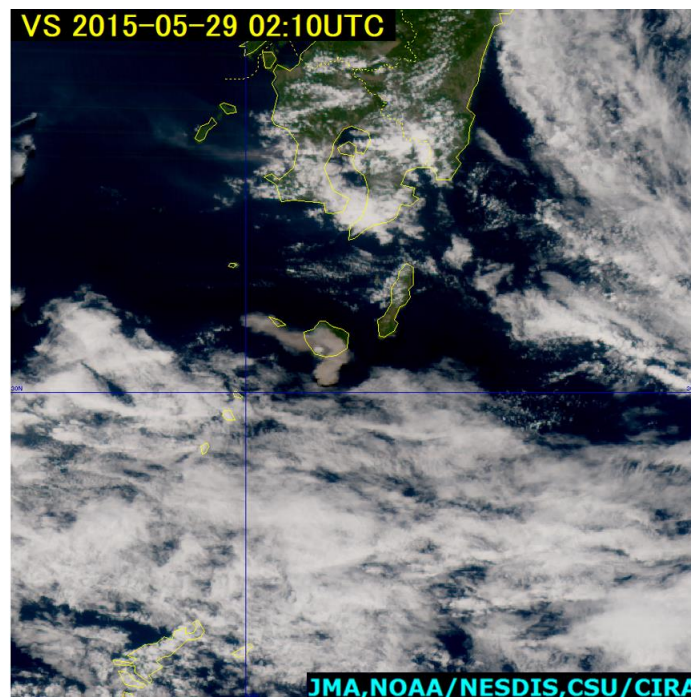

Fig. 7-4-1. B03 visible image for 09:30 UTC on 9 June 2015

Figure 7-4-2 shows Ash RGB composite image facilitating discrimination between volcanic ash and gas. It was made by combining a difference image of B13-B15 which lowers the temperature in the presence of volcanic ashes (Fig. 7-4-3) and a difference image of B13-B11 which lowers the temperature in the presence of volcanic gases (Fig. 7-4-4). The Ash RGB image shows volcanic ashes in magenta, volcanic gases in yellow-green and the overlap of the both in yellow. Following the eruption of Kuchinoerabu Island, volcanic ashes and gases were both seen.
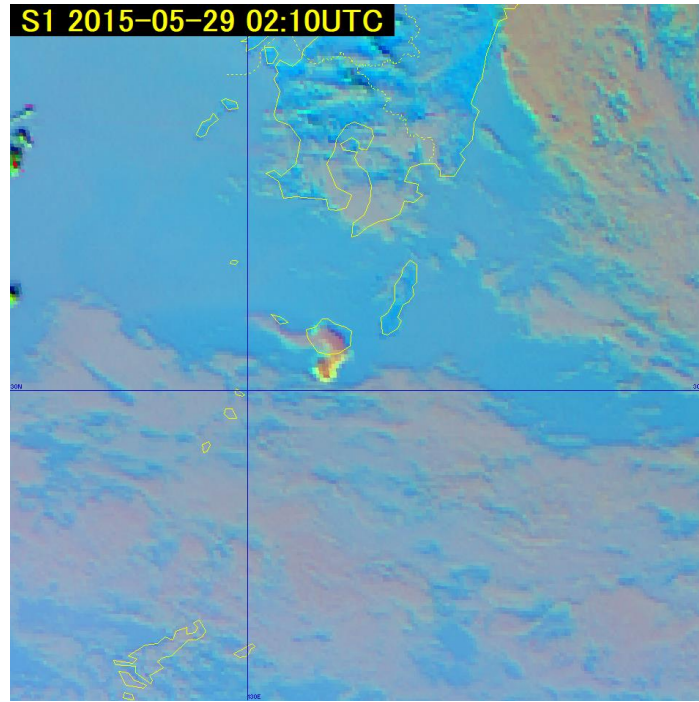
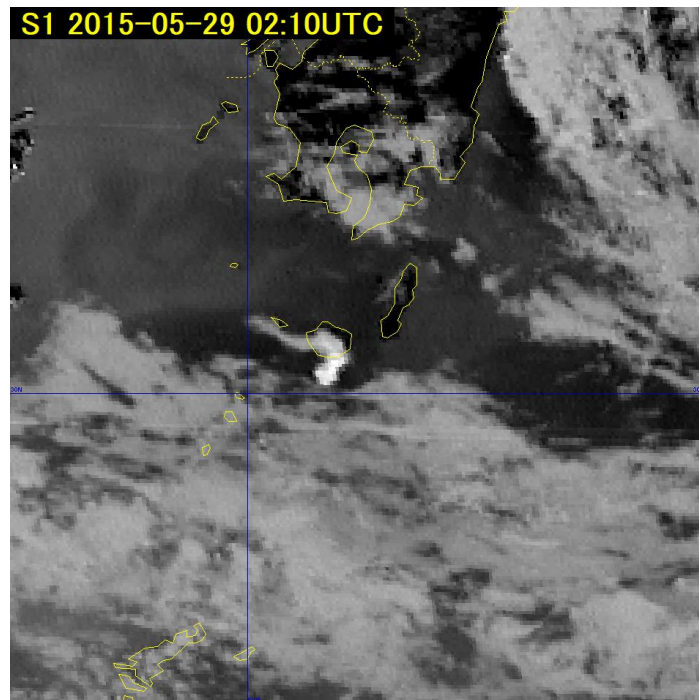Fig. 7-4-2. Ash RGB composite image at 02:10 UTC on 29 May 2015

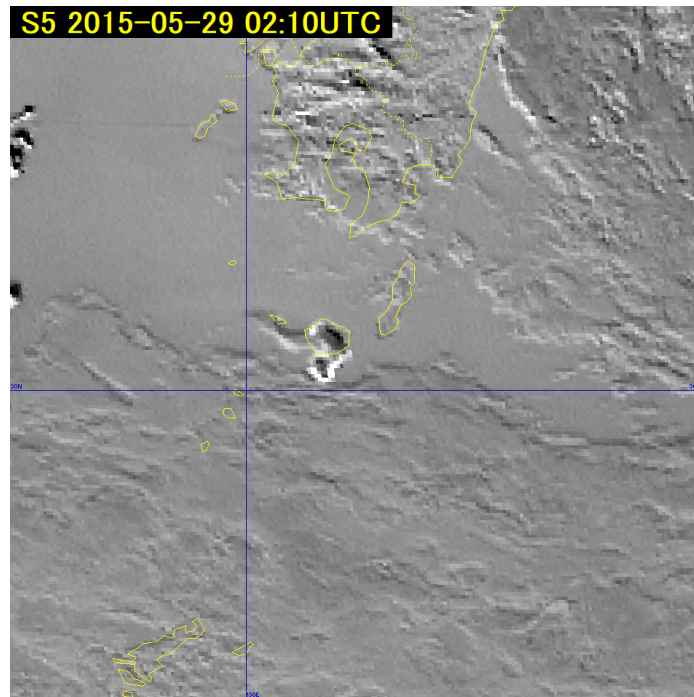Fig. 7-4-3. Difference image of Band 15 and Band 13 at 02:10 UTC on 29 May 2015

Fig. 7-4-4. Difference image of Band 13 and Band 11 at 02:10 UTC on 29 May 2015

7.5.Forest Fires and Smoke

Small-scale forest fires are difficult to identify from satellite imagery due to limited spatial resolution and observation frequency. However, the origins of larger-scale fires lasting several days can be estimated from smoke in visible imagery and hotspots in near-infrared and infrared imagery (Section 1.2: Characteristics of Each Observation Band).

Smoke from fires is often seen in visible imagery, spreading widely in a veil-like form with land and sea identifiable below, while smoke in infrared imagery cannot be seen without significant absorption. Based on these characteristics, smoke can be discriminated from clouds. The image below depicts a fire in Siberia at 07:00 on 30 April 2016. The rectangle in True Color Reproduction image contains a transparent grey area with land visible below (Fig. 7-5-1, top left), which is not seen in Band 13 image Fig. (Fig. 7-5-1, top right). Band 7 image also shows black fire hotspots (Fig. 7-5-1, bottom left), which are not observed in Band 13 image. From these observations, the grey region to the top left of Fig. 7-5-1 is assumed to be smoke capable of reaching Japan.
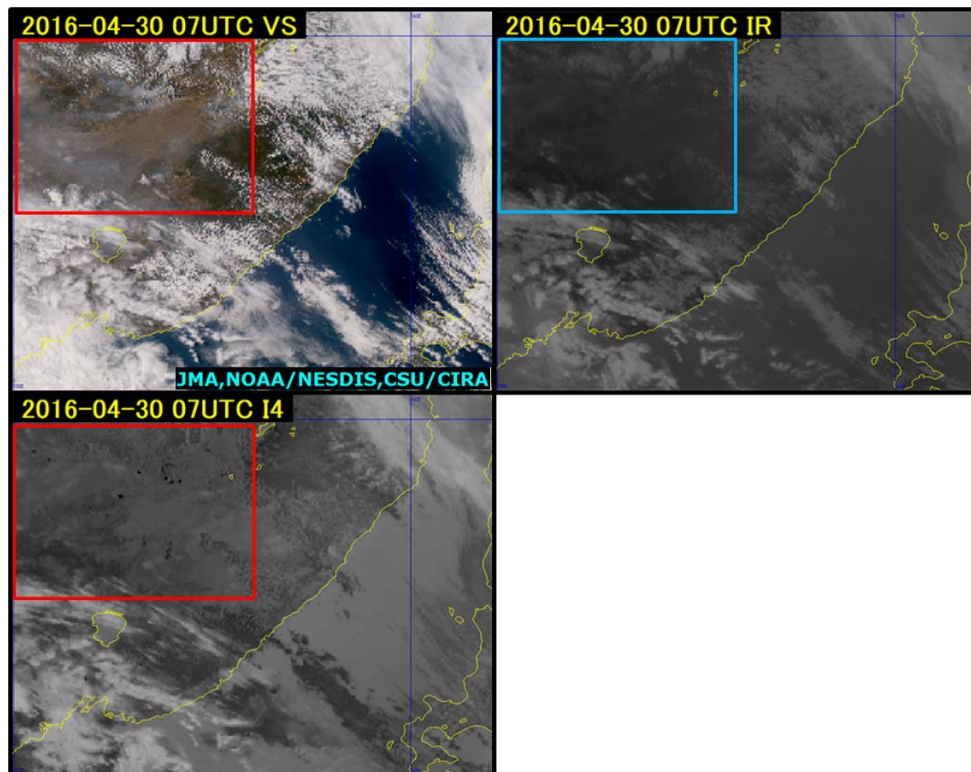

Fig. 7-5-1. Fire in Siberia at 07:00 UTC on 30 April 2016
Top left: True Color Reproduction; top right: B13 infrared; bottom left: B07 infrared

Figure 7-5-2 a from 06:00 UTC on 18 May 2016 shows a True Color Reproduction image with a white region not seen in the infrared image of Fig. 7-5-2 b. The shape/color differences from the lower clouds typically seen over the Sea of Japan suggest the presence of smoke moving from Hokkaido toward the Hokuriku and Kanto regions in correspondence with wind-direction and speed data based MSM 850-hPa analysis.
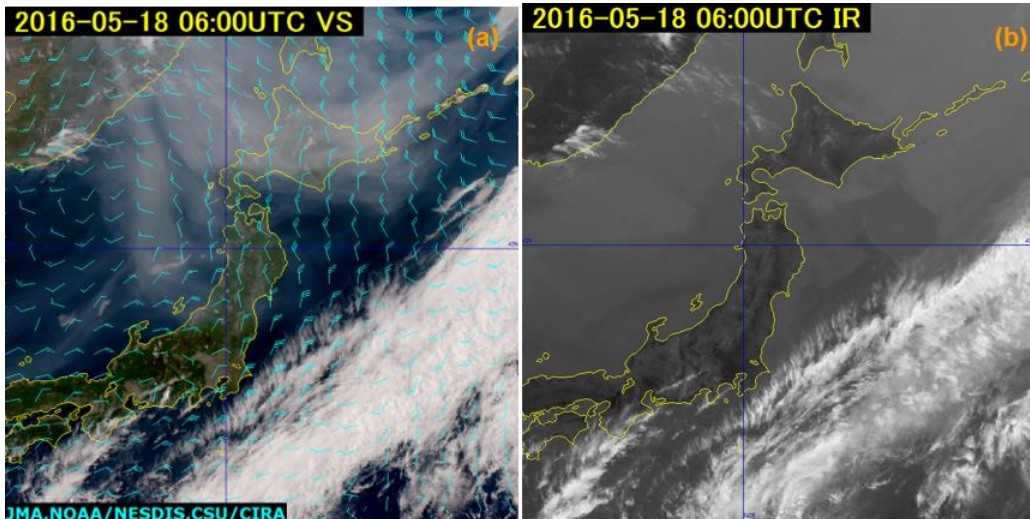
Fig. 7-5-2 Smoke from a wildfire at 06:00 UTC on 18 May 2016.
(a)True Color Reproduction image (left). (b) B13 infrared imagery (right).

Areas of burning can be determined from changes in vegetation cover. Figures 7-5-3(a)/(b) show changes relating to a fire around Lake Khanka in northeastern China. Natural Color RGB composite imagery (Fig. 7-5-3(a)) reveals a dark-brown region not seen on 14 October in northern and eastern parts of the encircled area, and many more hotspots (black dots) are seen around the lake on 25 October than on 14 October in the Band 7 imagery of Fig. 7-5-3(b). Accordingly, the region is assumed to have undergone fire damage.
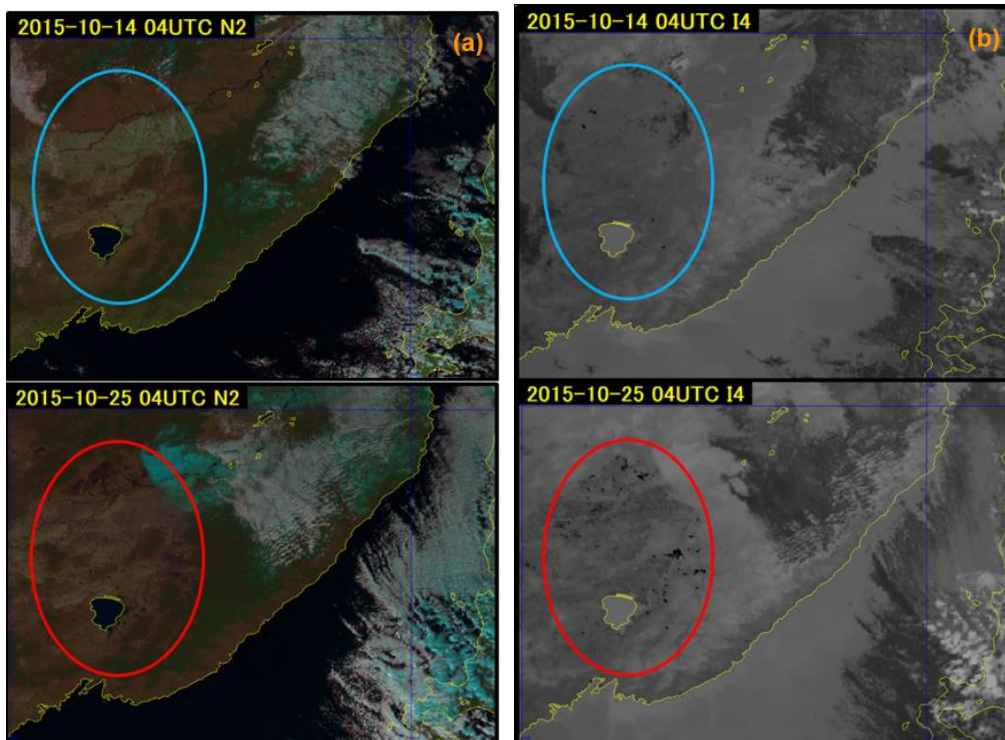

Fig. 7-5-3 Impact of wildfire around Lake Khanka.
(a) Natural Color RGB imagery (left). (b) B07 infrared imagery

Smoke from frequent major dry-season forest fires occurring in Indonesia over periods of months since the summer of 2015 is visible in satellite imagery. Figure 7-5-4(a) shows True Color Reproduction imagery revealing a thin-brown region extending from Borneo to Sumatra (not seen in the Band 13 infrared imagery of Fig. 7-5-4(b)) indicating forest fire smoke.
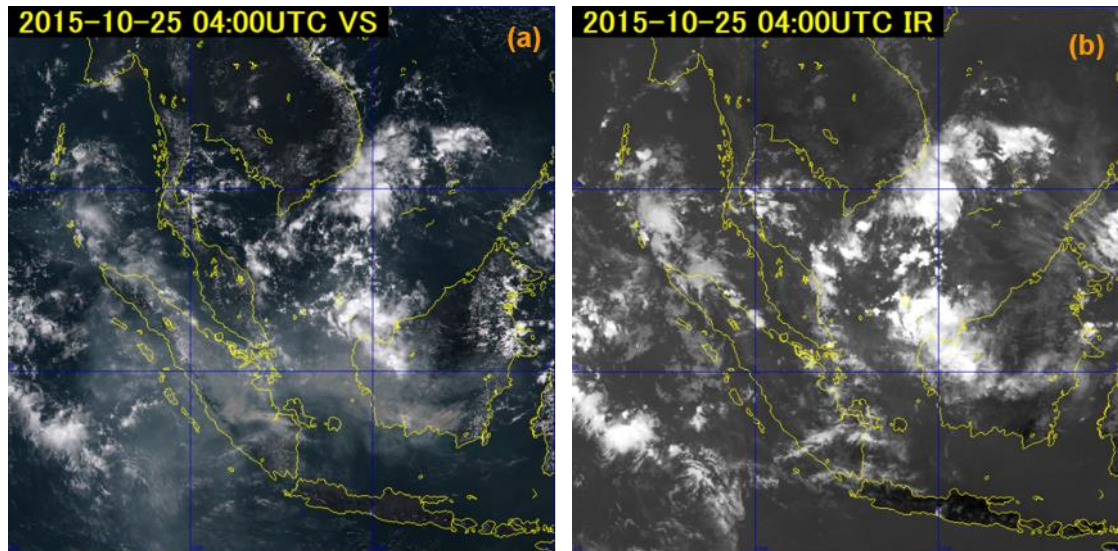

Fig. 7-5-4 Fire in Indonesia at 04:00 UTC on 25 October 2015.

(a) True Color Reproduction RGB composite image (left).

(b) B13 infrared image (right).

7.6. Sun Glint

Sun glint appears as bright reflections on the surfaces of large lakes and sea areas in visible and infrared imagery, with seasonal and temporal variations.

Its scale depends on the positions of the sun, the earth and the relevant satellite with minor latitudinal differences (up to approx. 30 km) and larger longitudinal differences (40 – 120 km). Size and reflection intensity depend on water conditions, being the smallest on relatively still sea surfaces with gentle winds and larger/darker with strong winds, thereby allowing determination of sea surface conditions.

Figure 7-6-1 shows the mechanism of sun glint on a steady sea surface acting as a mirror at Point B directly incidental to the satellite sensor, whereas the sunlight reflected at Point A is not directly incidental. Thus, the satellite sees the reflection at Point B directly and produces the brightest region of sun glint in visible imagery. Sun glint moves from east to west during the daytime in imagery. On a seasonal basis, the center moves from latitudes of 11.75° north to 11.75° south around 140° east.
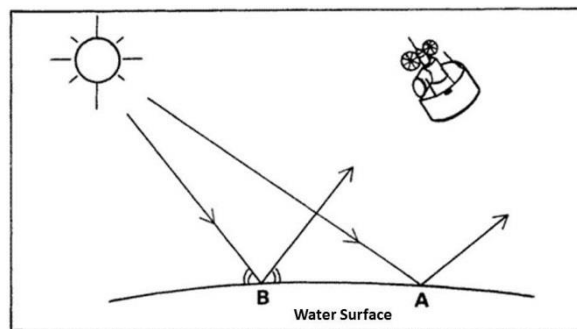

Fig. 7-6-1. Sun glint mechanism

The visible image in Fig 7-6-2 shows a bright part around 10° north latitude and 150° east longitude (arrow) representing sun glint. Small and bright glint areas like this suggest a still sea surface. From the observation time just after 10:00 JST, the sun glint is at around 150° east longitude. Figure 7-6-3 showing True Color RGB composite imagery for the same time period indicates bright sun glint over the sea surface.
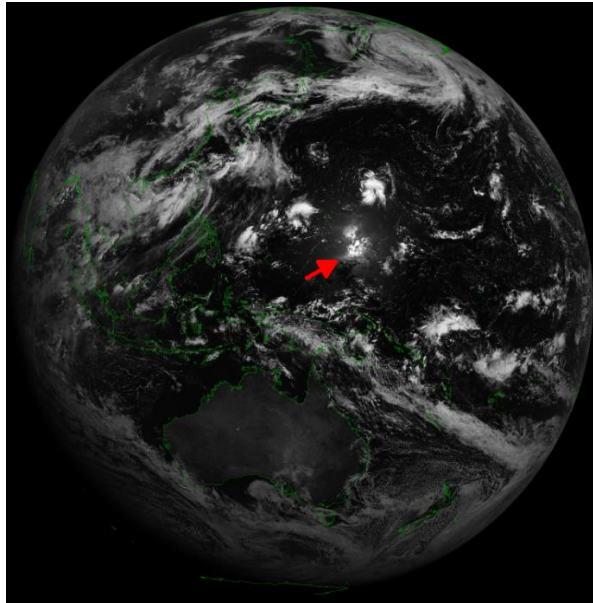
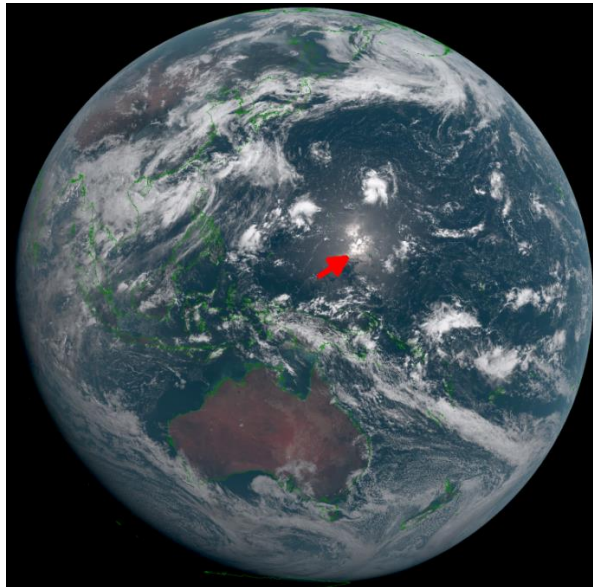Fig. 7-6-2. Visible image for 01:20 UTC on 19 July 2015

Fig. 7-6-3. True Color RGB composite image for 01:20 UTC on 19 July 2015

In December, sun glint is positioned in the Southern Hemisphere as in Fig. 7-6-4. In observation just before 09:00 JST, it is seen at 10° south latitude and 160° east longitude (arrow). Figure 7-6-5 shows True Color RGB composite image for the same time period, indicating Southern Hemisphere sun glint as in visible image.
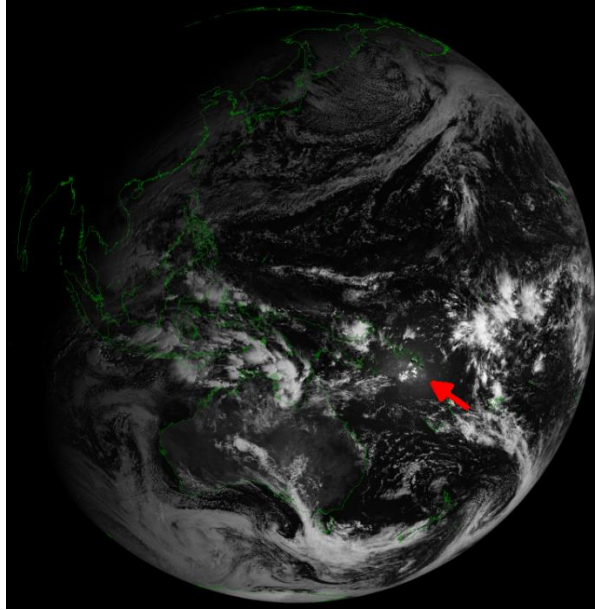
Fig. 7-6-4. Visible image for 23:40 UTC on 19 December 2015

Fig. 7-6-5. True Color RGB composite image for 23:40 UTC on 19 December 2015

Reference:

− E. G. Emecen, G. Kara, F. Erdoğmuş and R. Gardashov, 2005: The Determination of Sunglint Locations on the Ocean Surface by Observation from Geostationary Satellites, TAO, Vol. 17, No. 1, 253-261., Retrieved April 1, 2024, from http://tao.cgu.org.tw/index.php/articles/archive/space-science/item/download/643_35eeb72969bfb86f14dfd41a0317dbbd

Chapter 7.   Other Phenomena

7.7. Solar Eclipses

Solar eclipses are difficult to observe at all angles of incidence because their visibility is influenced by weather conditions and location. However, geostatic meteorological satellites capture lunar shadows projected onto observation areas without fail.

True Color RGB composite imagery for 02:00 UTC on 9 March 2016 (Fig. 7-7-1) shows a black lunar shadow over the Pacific. The shadow itself and the broad cloud distribution here are much clearer than in observation from the ground surface.
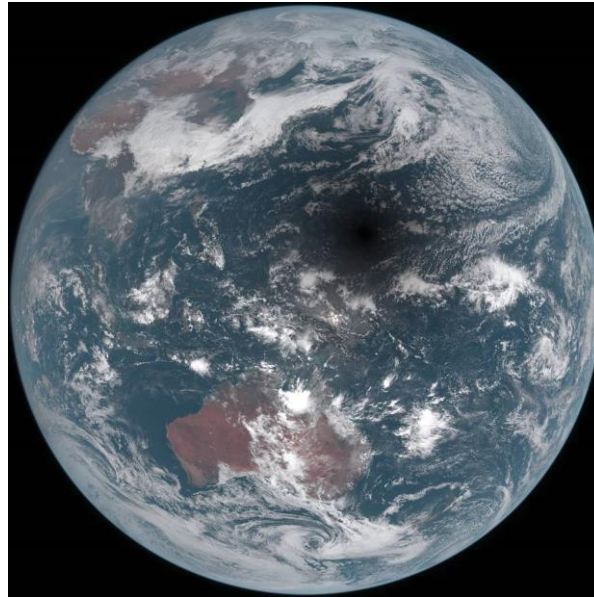

Fig. 7-7-1. True Color RGB imagery for 02:00 UTC on 9 March 2016

B03 from 0.64 μm visible imagery is enlarged in Fig. 7-7-2 a to centralize the shadow, and Fig. 7-7-2 b shows isoline reflectance. The darker center of the round shadow is clearly visible around 12° north latitude and 148° east longitude.
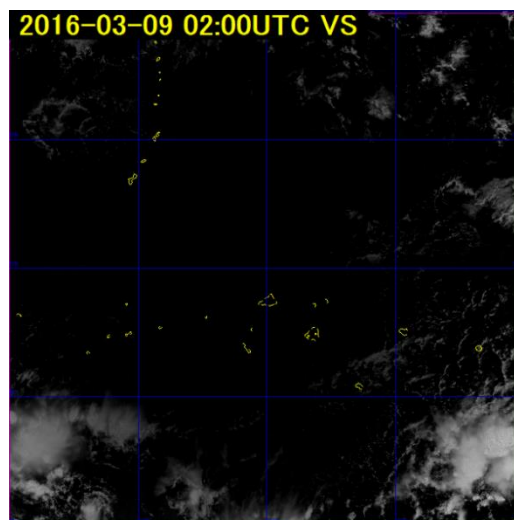

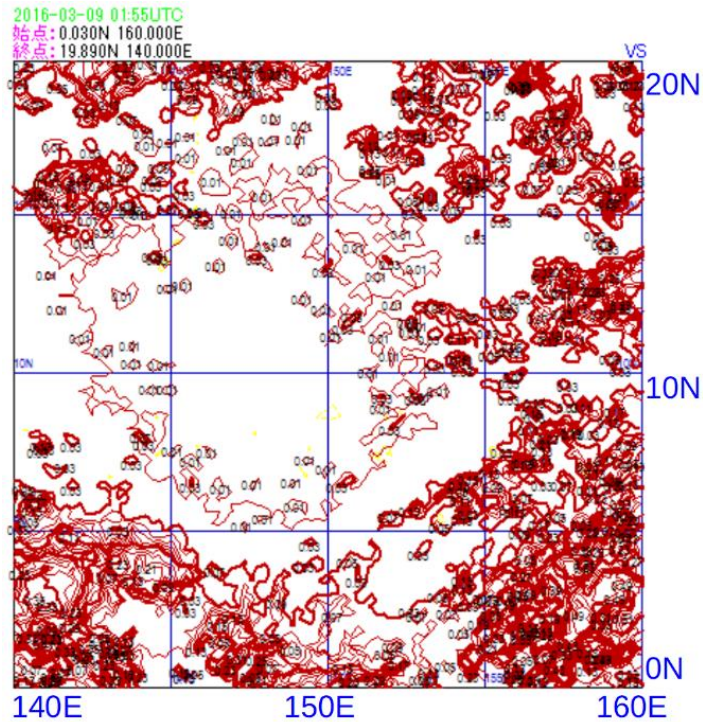Fig. 7-7-2(a) B03 visible imagery for 02:00 UTC on 9 March 2016

Fig. 7-7-2(b) Isoline display of Fig. 7-7-2(a) with round area of low reflectance

Figures 7-7-3(a)-(c) show enlarged Night Microphysics RGB composite imagery for the area around Borneo at the time of a solar eclipse. While Fig. 7-7-3 does not allow cloud discrimination due to the reflection of visible light over the cloud area, the imagery in b and c shows visible light being obtruded by the eclipse, enabling visualization of cloud in the same color as at nighttime. A thick cloud area associated with rainfall is seen in orange with yellow dots in region **A**, and fog and lower clouds are seen in bluish-white in region **B**.
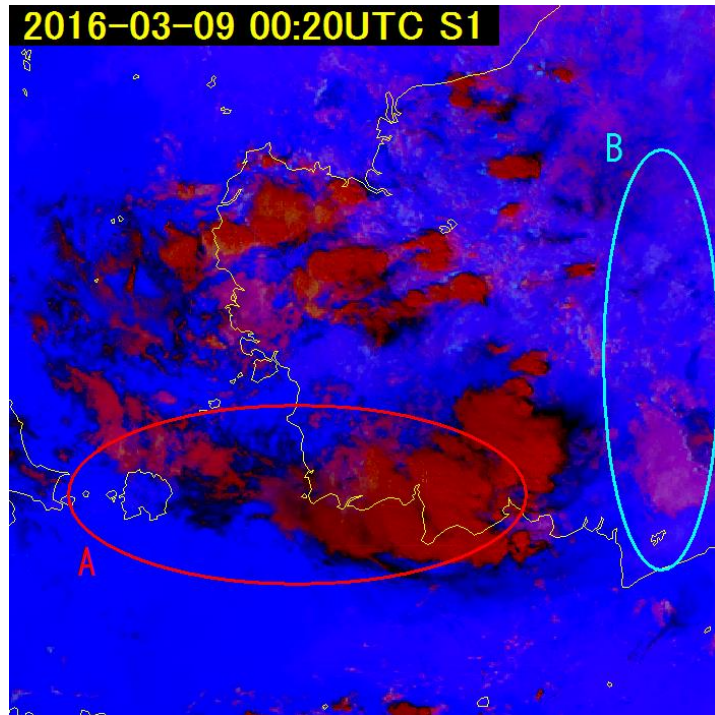
Fig. 7-7-3(a). Night Microphysics RGB composite imagery for 00:20 UTC on 9 March 2016
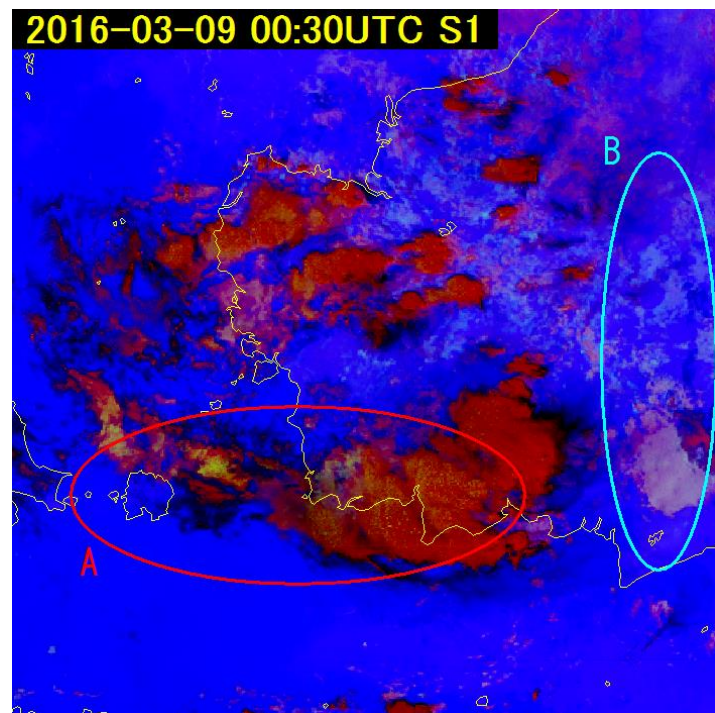

Fig. 7-7-3(b). Night Microphysics RGB composite imagery for 00:30 UTC on 9 March 2016
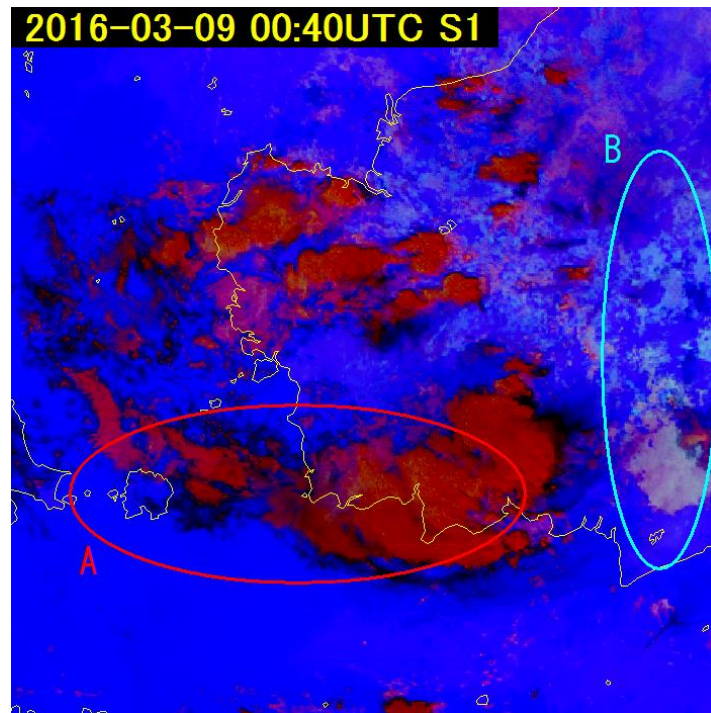
Fig. 7-7-3(c). Night Microphysics RGB composite imagery for 00:40 UTC on 9 March 2016